Chinese Chemical Letters 32 (2021) 2539–2543

Contents lists available at ScienceDirect

Chinese Chemical Letters

journal homepage: www.elsevier.com/locate/cclet

Communication

In-situ construction of amorphous/crystalline contact Bi_2S_3/Bi_4O_7 heterostructures for enhanced visible-light photocatalysis

Feihu Mu[a,1], Benlin Dai[a,1], Wei Zhao[a], Xiaofan Yang[a], Xiaolong Zhao[b], Xujing Guo[c,*]

[a] Jiangsu Key Laboratory for Chemistry of Low-Dimensional Materials, Jiangsu Collaborative Innovation Center of Regional Modern Agriculture and Environmental Protection, School of Chemistry and Chemical Engineering, Huaiyin Normal University, Huaian 223300, China
[b] Department of Mechanical Engineering, The University of Hong Kong, Hong Kong, China
[c] College of Resources and Environment, Chengdu University of Information Technology, Chengdu 610225, China

ARTICLE INFO

Article history:
Received 5 September 2020
Received in revised form 12 November 2020
Accepted 10 December 2020
Available online 16 December 2020

Keywords:
Photocatalysis
Cr(VI) reduction
Heterojunction
Bismuth-based oxide
Bismuth-based sulfide

ABSTRACT

Constructing a heterojunction photocatalyst is a significant method to enhance photocatalytic activity because it can promote the separation of photogenerated carriers. Herein, amorphous/crystalline contact Bi_2S_3/Bi_4O_7 heterostructure was successfully synthesized by *in-situ* sulfidation of Bi_4O_7. The amorphous Bi_2S_3 is diffused on the surface of Bi_4O_7 rod, enhancing the visible light response and improving the transport of photogenerated carriers. Various characterizations confirm that the rapid separation of photogenerated carriers leads to increased photocatalytic performance. The optimized Bi_2S_3/Bi_4O_7 heterostructure photocatalyst (BiS-0.15) exhibits the highest Cr(VI) reduction (0.01350 min^{-1}) and RhB oxidation (0.08011 min^{-1}) activity, which is much higher than that of pure Bi_4O_7 and Bi_2S_3/Bi_4O_7 mixture under visible light irradiation. This work provides new insights into the construction of efficient novel photocatalysts.

Nowadays, the discharge of wastewater containing heavy metal ions (such as Cr(VI), Hg(II), and Pb(II)) and organic pollutants (such as toxic dyes, phenol, and naphthalene) is causing more and more environmental problems [1,2]. Therefore, it is particularly important to remove these pollutants from wastewater. In the past few years, photocatalytic technology has been increasingly used in wastewater treatment [3–8]. However, many semiconductor photocatalysts with wide bandgap (E_g) only absorb and utilize the ultraviolet region, which contributes 3%–5% to the solar spectrum [9–11]. To use sunlight more efficiently, it is required to develop narrow Eg photocatalysts with a visible light response, because the visible light region accounts for about 43% of sunlight [12]. Therefore, various new photocatalysts that can make full use of solar energy have been designed and explored [13–16].

As a versatile photocatalyst, bismuth-based semiconductor materials, such as $BiVO_4$, Bi_2MoO_6, BiOCl, BiOBr, BiOI, $Bi_2O_2CO_3$, $BiOIO_3$, and bismuth-based oxides, are widely used in photocatalytic processes [17–25]. In particular, bismuth-based oxides (*e.g.*, α-Bi_2O_3, β-Bi_2O_3, γ-Bi_2O_3, δ-Bi_2O_3, Bi_2O_4, Bi_2O_{2-x}, Bi_4O_7, Bi_6O_7) have a strong visible light response, because the Bi-O system contains intermediate phases and the 6 s orbital of Bi^{3+} can overlap the O 2p orbital [26–28]. However, the recombination rate of carriers in these bismuth-based oxides is relatively fast, which hinders their photocatalytic activity. To solve this problem, constructing bismuth-based oxide heterojunction materials is an effective method [29–32]. For example, Deng *et al.* synthesized $BiOCl/Bi_2O_3$/rGO heterojunction for photocatalytic treatment of real industrial wastewater. Due to the reasonable band gap match between BiOCl and Bi_2O_3, this Z-scheme $BiOCl/Bi/Bi_2O_3$/rGO heterojunction exhibited excellent photocatalytic performance [33]. Hong *et al.* synthesized β-Bi_2O_3@g-C_3N_4 heterojunction by self-assembly method. This Z-scheme heterojunction photocatalyst can significantly extend the lifetime of carriers and promote the separation of carriers. As a result, the sample containing 5 wt% g-C_3N_4 (5% CN@BO) can efficiently degrade tetracycline (k = 0.0311 min^{-1}) [34]. However, there are only a few studies on Bi_4O_7 heterojunction [26,35–38], which need further exploration.

Herein, amorphous/crystalline contact Bi_2S_3/Bi_4O_7 heterostructure was constructed by *in-situ* sulfidation of Bi_4O_7 (Fig. 1a). Briefly, 1.20 g $NaBiO_3 \cdot 2H_2O$ was dispersed into 40 mL water and put into a 50 mL autoclave, which was then heated at 180 °C for 6 h. The resulting powders were collected, and taken into a crucible and heated at 250 °C for 2 h with a heating rate of 2 °C/min. After cooling, the Bi_4O_7 product was prepared. Then, 0.1 mmol Bi_4O_7 was dispersed into 25 mL water and sonicated for 15 min.

* Corresponding author.
E-mail address: gxj530520@126.com (X. Guo).
[1] These authors contributed equally to this work.

https://doi.org/10.1016/j.cclet.2020.12.016

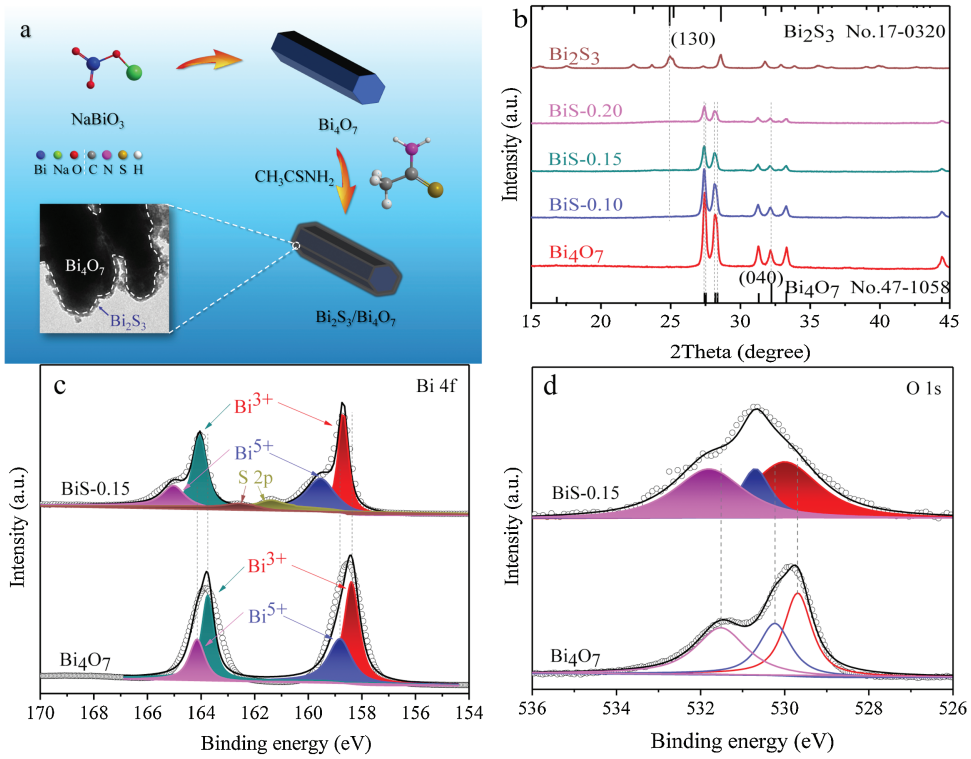

Fig. 1. (a) Schematic diagram of Bi_2S_3/Bi_4O_7 preparation. (b) XRD patterns of different photocatalysts. XPS spectra of Bi_4O_7 and BiS-0.15: (c) Bi 4f, (d) O 1s.

Subsequently, 10 mL thioacetamide solution (0.010 mmol) was added dropwise and reacted at 50 °C for 5 h with stirring. Finally, the resulting Bi_2S_3/Bi_4O_7 product was collected by centrifugation and labeled as BiS-0.10. In the case of other conditions unchanged, change the amount of thioacetamide solution to 15 mL (0.015 mmol) and 20 mL (0.020 mmol), the resulting products were labeled as BiS-0.15 and BiS-0.20, respectively. In this heterostructure, the amorphous Bi_2S_3 boost the visible light response of Bi_4O_7 and accelerate the photogenerated carrier transport. Under visible light irradiation, the amorphous/crystalline contact Bi_2S_3/Bi_4O_7 exhibits excellent photocatalytic Cr(VI) reduction and rhodamine B (RhB) oxidation activity.

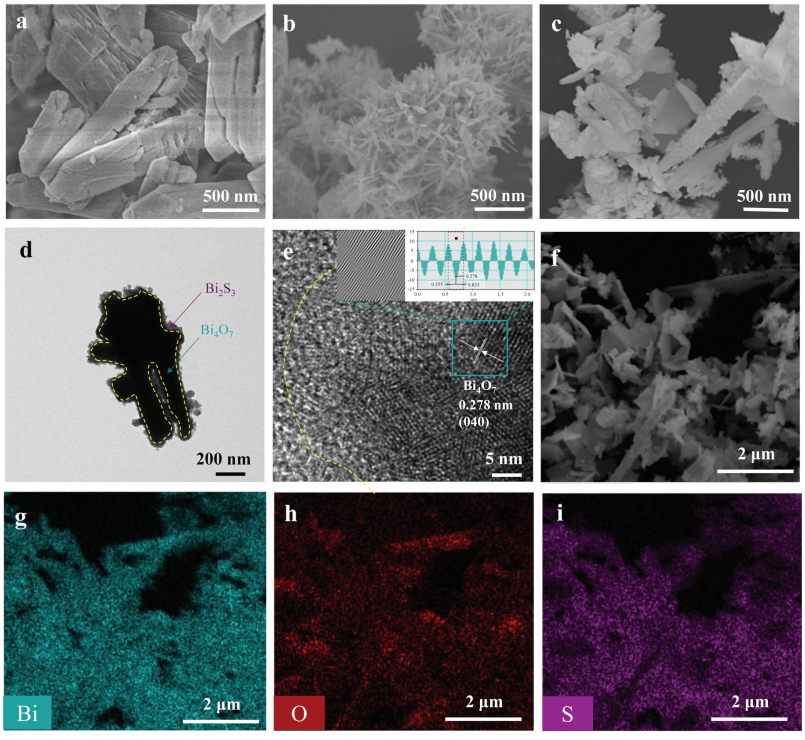

Fig. 2. FESEM images of (a) Bi_4O_7, (b) Bi_2S_3, (c) BiS-0.15, TEM (d) and HRTEM (e) images of BiS-0.15, (f) FESEM images of BiS-0.15 and SEM-EDS elemental mapping of (g) Bi element, (h) O element, and (i) S element.

The crystal structures of different photocatalysts were studied by XRD. In Fig. 1b, Bi_4O_7 exhibits five characteristic XRD diffraction peaks at 27.4°, 27.5°, 28.1°, 28.3° and 32.2°, which can be indexed to (22), (2), (22), (222) and (040) crystal planes of triclinic Bi_4O_7 phase (JCPDS No. 47-1058) [26,39], respectively. For Bi_2S_3, all peaks correspond to the orthorhombic Bi_2S_3 phase (JCPDS No. 17-0320) [40–42]. In particular, the XRD patterns of the BiS-0.10, BiS-0.15, and BiS-0.20 composites show no characteristic peaks of Bi_2S_3, because Bi_2S_3 is amorphous in these composites. Moreover, with the increase of Bi_2S_3 content, the relative intensity of the Bi_4O_7 diffraction peak in Bi_2S_3/Bi_4O_7 composite decreases, and the relative intensity of the Bi_4O_7 diffraction peak in BiS-0.20 is the lowest.

The surface chemical state and composition of different photocatalysts were further detected by XPS. The survey spectra (Fig. S1 in Support information) indicate that only Bi and O elements are present in Bi_4O_7, while BiS-0.15 is composed of Bi, O, and S elements. In Fig. 1c (Bi 4f spectra), both Bi $4f_{5/2}$ and Bi $4f_{7/2}$ can be divided into double peaks. For Bi_4O_7, the peaks at 158.3 and 163.7 eV are assigned to Bi^{3+}, while the peaks at 158.8 and 164.2 eV are ascribed to Bi^{5+} [36,43]. However, the characteristic peaks of Bi^{3+} are 158.7 and 164.1 eV, and the peaks of Bi^{5+} are 159.5 and 164.9 eV over BiS-0.15. Noticeably, the peaks at 161.3 and 162.5 eV in BiS-0.15 are attributed to S 2p [44,45], which confirms the presence of Bi_2S_3 in BiS-0.15. In Fig. 1d, the O 1s peak of Bi_4O_7 can be divided into three peaks, located at 529.7, 530.4, and 531.5 eV, respectively. The XPS peak at 529.7 eV belongs to lattice oxygen, while the peaks at 530.4 and 531.5 eV are ascribed to chemically adsorbed oxygen and physically adsorbed oxygen, respectively [26,46]. However, these O 1s peaks are located at 529.9, 530.6, and 531.8 eV in BiS-0.15, respectively. Therefore, compared with Bi_4O_7, the peaks of Bi 4f and O 1s in BiS-0.15 are shifted to high values, which demonstrates that there is a strong interaction between Bi_4O_7 and Bi_2S_3.

The morphologies of Bi_4O_7, Bi_2S_3, and BiS-0.15 were explored by field emission scanning electron microscopy (FESEM). Bi_4O_7 exhibits a rod-like morphology (Fig. 2a), while Bi_2S_3 displays a needle-like morphology (Fig. 2b). Fig. 2c shows the typical FESEM image for BiS-0.15. Compared with the smooth surface of pure Bi_4O_7, the surface of BiS-0.15 becomes very rough, further indicating that Bi_2S_3 is formed on the surface of Bi_4O_7 after reaction with thioacetamide. Moreover, the microstructure of BiS-0.15 was further researched by TEM. In Fig. 2d, a layer of Bi_2S_3 is in-situ formed on the surface of rod-like Bi_4O_7. In the HRTEM image of BiS-0.15 (Fig. 2e), the fringe with a lattice spacing of 0.278 nm is characteristic to the (040) crystal plane of Bi_4O_7. This HRTEM image also confirms that Bi_2S_3 is amorphous, which is in accordance with the XRD pattern. Additionally, in the scanning electron microscopy-energy dispersive X-ray spectrometry (SEM-EDS) elemental mapping (Figs. 2f–i), the Bi, O, and S elements in BiS-0.15 are evenly dispersed, demonstrating that Bi_2S_3 is uniformly dispersed on the surface of Bi_4O_7.

The surface area of the obtained samples was evaluated by N_2 adsorption-desorption. In Fig. 3a, all the samples exhibit type IV isotherms. The BET surface areas of Bi_4O_7, BiS-0.10, BiS-0.15, and BiS-0.20 are 2.94, 7.95, 8.76, and 9.32 m^2/g, respectively. Therefore, the surface area of the Bi_2S_3/Bi_4O_7 heterojunction is greater than that of Bi_4O_7, which is beneficial to the photocatalytic reaction. Moreover, the optical characteristic of as-prepared samples was studied by UV–vis diffuse reflectance spectroscopy (DRS) (Fig. 3b). In the visible light region, Bi_4O_7 has strong light absorption, and its absorption edge is estimated to be about 700 nm, while Bi_2S_3 has stronger light absorption than that of Bi_4O_7. The light absorption properties of BiS-0.10, BiS-0.15, and BiS-0.20 are between Bi_4O_7 and Bi_2S_3. Besides, the colors of Bi_4O_7 and Bi_2S_3 are brownish-red and black (Fig. 3b, inset), respectively. With the increase of Bi_2S_3 content, the color of Bi_2S_3/Bi_4O_7 heterojunction gradually becomes darker. According to the curve of Fig. 3c ($(\alpha hv)^2$ *versus* energy), the band gaps (E_g) of Bi_4O_7 and Bi_2S_3 are estimated to be 1.82 and 1.35 eV, respectively.

The photocatalytic performance of Bi_4O_7, Bi_2S_3, BiS-0.10, BiS-0.15, BiS-0.20, and Bi_2S_3/Bi_4O_7 physical mixture was studied by Cr(VI) reduction and RhB oxidation in water. To confirm the important roles of photocatalyst, blank experiments (in the absence of photocatalysts, self-degradation) were also performed under identical conditions. From Fig. 3d, it can be observed that the self-degradation process of Cr(VI) can be neglected. Meanwhile, the Cr(VI) reduction rates of pristine Bi_4O_7 and pristine Bi_2S_3 are

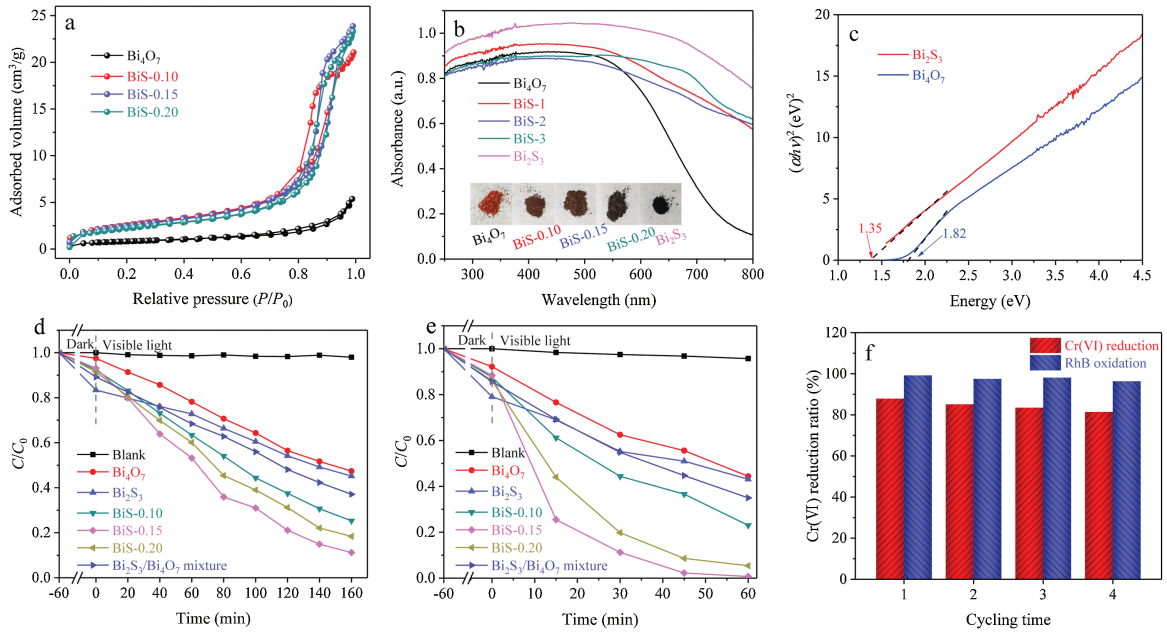

Fig. 3. (a) Nitrogen adsorption-desorption isotherms, (b) UV–vis DRS (the inset is the digital pictures), (c) the curve of $(\alpha hv)^2$ against energy (hv), the result of photocatalytic (d) Cr(VI) reduction and (e) RhB oxidation, (f) four recycling runs of BiS-0.15 for Cr(VI) reduction and RhB oxidation.

51.3% and 45.8%, respectively. After the incorporation of Bi_2S_3, the degradation activity of BiS-0.10 increases significantly to 72.5%. Further increasing the amount of Bi_2S_3, the Cr(VI) reduction rates of BiS-0.15 and BIS-0.20 are 87.9% and 79.7%, respectively. In particular, BiS-0.15 exhibits the highest activity of Cr(VI) reduction. Noticeably, the photocatalytic activity of the Bi_2S_3/Bi_4O_7 heterojunction is much higher than that of the Bi_2S_3/Bi_4O_7 physical mixture (58.4%). These experimental results demonstrate that loading Bi_2S_3 on the surface of Bi_4O_7 can promote Cr(VI) reduction, and the optimal dosage of Bi_2S_3 is 15%. In addition, this Cr(VI) reduction results conform to the *pseudo*-first-order dynamics model: $\ln(C_0/C_t) = k_{app}t$ [47]. In Fig. S2 (Supporting information), the apparent reaction rate constants (k_{app}) of Bi_4O_7, Bi_2S_3, BiS-0.10, BiS-0.15, BiS-0.20 and Bi_2S_3/Bi_4O_7 mixture are 0.00467, 0.00396, 0.00819, 0.01350, 0.01023 and 0.00550 min^{-1}, respectively.

In Fig. 3e, the self-degradation rate of RhB was only 4.3%, while the RhB oxidation rates of pristine Bi_4O_7 and pristine Bi_2S_3 are 51.8% and 45.5%, respectively. After the incorporation of Bi_2S_3, the RhB oxidation rate of BiS-0.10 increases significantly to 73.7%. In particular, BiS-0.15 exhibits the highest activity of photocatalytic RhB oxidation (99.2%). Further increasing the amount of Bi_2S_3, the oxidation rate of BIS-0.20 is reduced to 93.7%, which is similar to the result of Cr(VI) reduction. Noticeably, the photocatalytic RhB oxidation activity of the Bi_2S_3/Bi_4O_7 heterojunction is much higher than that of the Bi_2S_3/Bi_4O_7 physical mixture (59.1%). Moreover, these RhB oxidation results also conform to the *pseudo*-first-order dynamics model. In Fig. S3 (Supporting information), the apparent reaction rate constants k_{app} of Bi_4O_7, Bi_2S_3, BiS-0.10, BiS-0.15, BiS-0.20 and Bi_2S_3/Bi_4O_7 mixture are 0.01154, 0.01009, 0.02124, 0.08011, 0.04768 and 0.01531 min^{-1}, respectively.

In addition, the stability of the photocatalytic reaction on BiS-0.15 was evaluated. As shown in Fig. 3f, after four cycles, the photocatalytic Cr(VI) reduction rate of BiS-0.15 is 81.4%, and the rate is 92.6% of the initial rate. This indicates that BiS-0.15 has good stability in photocatalytic Cr(VI) reduction. Moreover, BiS-0.15 also shows high stability in photocatalytic RhB oxidation since the oxidation rate is still up to 96.3% after four cycles. Besides, the XRD pattern (Fig. S4 in Supporting information) of BiS-0.15 shows no significant difference, demonstrating that the BiS-0.15 photocatalyst is structurally stable after photocatalytic cycles.

The recombination rate of photogenerated carriers is an important parameter that affects the photocatalytic performance [48]. The PL spectra can provide information about carrier recombination. Fig. 4a exhibits the PL spectra of Bi_4O_7, BiS-0.10, BiS-0.15, and BiS-0.20 excited at 360 nm. The PL intensity of BiS-0.10, BiS-0.15, and BiS-0.20 is lower than that of Bi_4O_7, and BiS-0.15 has the lowest PL intensity. Therefore, the photogenerated carriers rapidly recombine over Bi_4O_7, while the photogenerated carriers over the Bi_2S_3/Bi_4O_7 heterostructures are effectively separated due to interfacial charge transfer.

In addition, photoelectrochemical techniques were employed to further study the interface charge separation of photocatalysts. As illustrated in Fig. 4b (transient photocurrent responses), the photocurrent density of Bi_4O_7 is low because of the rapid recombination of photogenerated carriers. The photocurrent intensity over BiS-0.15 is much higher than that over Bi_4O_7, BiS-0.10, and BiS-0.20, which indicates that the photogenerated carriers over BiS-0.15 can be separated rapidly. Fig. 4c describes the electrochemical impedance spectroscopy (EIS) Nyquist plots for Bi_4O_7, BiS-0.10, BiS-0.15, and BiS-0.20. As an observation, the arc radius of BiS-0.15 is smaller than that of Bi_4O_7, BiS-0.10, and BiS-0.20, demonstrating that BiS-0.15 possesses a lower charge carrier transfer resistance. Noticeably, these EIS characterization results are consistent with the PL and transient photocurrent responses characterization results. In addition, these characterization results also agree with the results of photocatalytic Cr(VI) reduction experiments.

Generally, reactive species are very important in the photocatalytic reaction process and directly determine the reaction mechanism. To study the reaction species of RhB oxidation, some trapping agents were added during the BiS-0.15 photocatalytic oxidation of RhB. Ammonium oxalate (AO), Benzoquinone (BQ), and isopropanol (IPA) were employed to trap h^+, $O_2^{\bullet-}$, and $^{\bullet}OH$, respectively, and the results are shown in Fig. 4d. After the trapping agent is added, the photocatalytic oxidation is partially suppressed, and the photocatalytic oxidation efficiency value is reduced. The

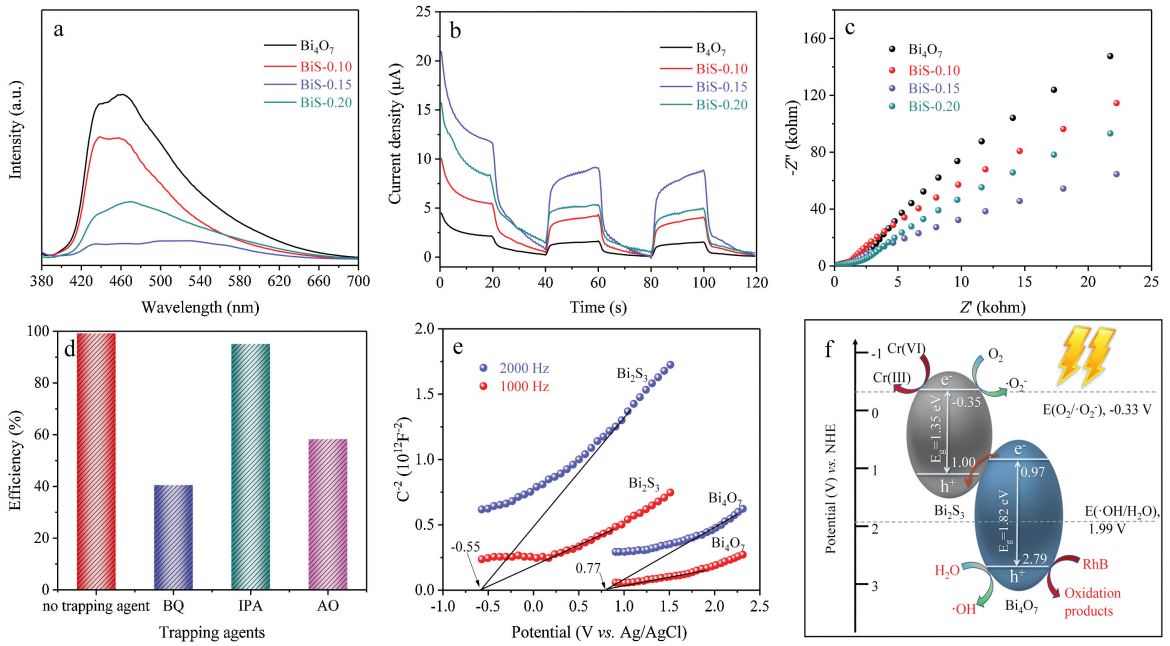

Fig. 4. (a) PL spectra, (b) transient photocurrent responses, (c) EIS Nyquist plots of Bi_4O_7, BiS-0.10, BiS-0.15, and BiS-0.20, (d) trapping experiments, (e) Mott-Schottky plots, (f) the proposed photocatalytic mechanism.

lower the photocatalytic oxidation efficiency value caused by the trapping agent, the more important the role of the corresponding reactive species in the photocatalytic oxidation. From Fig. 4d, it is observed that with the addition of AO and BQ, the photocatalytic oxidation efficiency value of RhB is significantly decreased, indicating that h^+ and $O_2^{\bullet-}$ are the main reactive species. However, IPA has almost no effect on the photocatalytic oxidation efficiency value, demonstrating that $^{\bullet}OH$ is not the main reactive species.

Furthermore, the band structures of Bi_4O_7 and Bi_2S_3 were measured by Mott-Schottky plots. In Fig. 4e, the flat band potentials (E_{FB}) of Bi_4O_7 and Bi_2S_3 are 0.77 and −0.55 V *vs.* Ag/AgCl, that is, 0.97 and −0.35 V *vs.* NHE, respectively. In general, the E_{FB} of an n-type semiconductor is close to the conduction band potential (E_{CB}) [49], so the conduction band potentials of Bi_4O_7 and Bi_2S_3 are estimated to be 0.97 and −0.35 V *vs.* NHE, respectively. Furthermore, the valence band potentials (E_{VB}) of Bi_4O_7 and Bi_2S_3 can be calculated to be 2.79 and 1.00 V *vs.* NHE, respectively, because the Eg of Bi_4O_7 and Bi_2S_3 is 1.82 and 1.35 eV (Fig. 3c), respectively.

If the electrons are transported from the CB of Bi_2S_3 to the CB of Bi_4O_7, while the holes are transported from the VB of Bi_4O_7 to the VB of Bi_2S_3. Since the E_{CB} of Bi_4O_7 (0.97 V *vs.* NHE) is more positive than the potential of $O_2/O_2^{\bullet-}$ (−0.33 V *vs.* NHE), the CB of Bi_4O_7 cannot generate $O_2^{\bullet-}$ radicals, conflicting the above reactive species trapping experiments. Therefore, it is concluded that electrons are transferred from the CB of Bi_4O_7 to the VB of Bi_2S_3. Based on the above analysis, a probable photocatalytic mechanism is proposed (Fig. 4f). Under visible light irradiation, both Bi_2S_3 and Bi_4O_7 are excited, thereby generating photogenerated electrons in their CB and photogenerated holes in their VB. The electrons on the CB of Bi_4O_7 tend to be transmitted to the VB of Bi_2S_3. The electrons in the CB of Bi_2S_3 react with O_2 to form $O_2^{\bullet-}$, while the holes in the VB of the Bi_4O_7 react with the H_2O to produce the $^{\bullet}OH$. Then, the formed $O_2^{\bullet-}$, $^{\bullet}OH$, e^-, and h^+ participate in the photocatalytic Cr(VI) reduction and RhB oxidation.

In summary, amorphous/crystalline contact Bi_2S_3/Bi_4O_7 photocatalyst was successfully constructed by the *in-situ* reaction of thioacetamide with Bi_4O_7. Compared with pure Bi_4O_7 and Bi_2S_3/Bi_4O_7 mixture, the amorphous/crystalline contact Bi_2S_3/Bi_4O_7 heterostructure shows superior photocatalytic Cr(VI) reduction and RhB oxidation activity. In particular, BiS-0.15 exhibits the highest photocatalytic activity, and the k_{app} of Cr(VI) reduction and RhB oxidation are 0.01350 and 0.08011 min^{-1}, respectively. The boosted photocatalytic activity is attributed to the effective separation of photogenerated carriers. The photocatalytic process is further supported by PL spectra, transient photocurrent responses, and EIS experimental results. This work is expected to provide valuable insights into the preparation of effective novel photocatalysts.

Declaration of competing interest

The authors declare that they have no known competing financial interests or personal relationships that could have appeared to influence the work reported in this paper.

Acknowledgments

This work was supported by the National Natural Science Foundation of China (Nos. 51808250, 51676082), the Natural Science Foundation of Jiangsu Province of China (Nos. BK20160430, BK20181070), the Jiangsu Planned Projects for Postdoctoral Research Funds of China (No. 1601179C), the Project Funded by China Postdoctoral Science Foundation (Nos. 2016M591757, 2017M610336), and Jiangsu Key Research and Development (R&D) Projects (Social Development, No. BE2020772).

Appendix A. Supplementary data

Supplementary material related to this article can be found, in the online version, at doi:https://doi.org/10.1016/j.cclet.2020.12.016.

References

[1] T. Wu, X. Liu, Y. Liu, et al., Coord. Chem. Rev. 403 (2020) 213097.
[2] H. Yu, L. Jiang, H. Wang, et al., Small 15 (2019) 1901008.
[3] X. Li, J. Yu, M. Jaroniec, Chem. Soc. Rev. 45 (2016) 2603–2636.
[4] Q. Guo, Z. Ma, C. Zhou, Z. Ren, X. Yang, Chem. Rev. 119 (2019) 11020–11041.
[5] Y.J. Gao, X.B. Li, H.L. Wu, et al., Adv. Funct. Mater. 28 (2018) 1801769.
[6] M. Zhu, Z. Sun, M. Fujitsuka, T. Majima, Angew. Chem., Int. Ed. 57 (2018) 2160–2164.
[7] T.H. Jeon, M.S. Koo, H. Kim, W. Choi, ACS Catal. 8 (2018) 11542–11563.
[8] F. Mu, B. Dai, W. Zhao, et al., Chin. Chem. Lett. 31 (2020) 1773–1781.
[9] M. Qamar, B. Merzougui, M.I. Ahmed, Z.H. Yamani, ACS Sustain. Chem. Eng. 6 (2018) 2112–2121.
[10] I. Velo-Gala, J. López-Peñalver, M. Sánchez-Polo, J. Rivera-Utrilla, Appl. Catal. B: Environ. 207 (2017) 412–423.
[11] Q. Chen, L. Chen, J. Qi, et al., Chin. Chem. Lett. 30 (2019) 1214–1218.
[12] R. Dong, Y. Hu, Y. Wu, et al., J. Am. Chem. Soc. 139 (2017) 1722–1725.
[13] Y. Sang, Z. Zhao, M. Zhao, et al., Adv. Mater. 27 (2015) 363–369.
[14] C. Jia, X. Zhang, K. Matras-Postolek, B. Huang, P. Yang, Carbon 139 (2018) 415–426.
[15] M.Z. Rahman, C.B. Mullins, Acc. Chem. Res. 52 (2018) 248–257.
[16] D. Yuan, M. Sun, S. Tang, et al., Chin. Chem. Lett. 31 (2020) 547–550.
[17] Y. Deng, L. Tang, C. Feng, et al., J. Hazard. Mater. 344 (2018) 758–769.
[18] F. Fu, H. Shen, W. Xue, et al., J. Catal. 375 (2019) 399–409.
[19] M. Ji, Z. Zhang, J. Xia, et al., Chin. Chem. Lett. 29 (2018) 805–810.
[20] M. Sun, S. Li, T. Yan, et al., J. Hazard. Mater. 333 (2017) 169–178.
[21] Z. Wei, T. Xinyue, W. Xiaomeng, et al., Chem. Eng. J. 361 (2019) 1173–1181.
[22] W. Zhao, J. Li, B. Dai, et al., Chem. Eng. J. 369 (2019) 716–725.
[23] I. Nabi, Z. Fu, K. Li, H. Cheng, L. Zhang, Chin. Chem. Lett. 30 (2019) 2225–2230.
[24] F. Chen, Z. Ma, L. Ye, et al., Adv. Mater. 32 (2020) 1908350.
[25] M. Li, S. Yu, H. Huang, et al., Angew. Chem. Int. Ed. 58 (2019) 9517–9521.
[26] M. Ye, W. Wei, L. Zheng, et al., J. Hazard. Mater. 365 (2019) 674–683.
[27] J. Di, X. Zhao, C. Lian, et al., Nano Energy 61 (2019) 54–59.
[28] R. Li, F. Xie, J. Liu, et al., Dalton Trans. 45 (2016) 9182–9186.
[29] J. Xiong, P. Song, J. Di, H. Li, Z. Liu, J. Mater. Chem. A 7 (2019) 25203–25226.
[30] M. Li, H. Huang, S. Yu, N. Tian, Y. Zhang, ChemCatChem 10 (2018) 4477–4496.
[31] W. Fang, W. Shangguan, Int. J. Hydrogen Energy 44 (2019) 895–912.
[32] W. Zhao, J. Zhang, F. Zhu, et al., Chem. Eng. J. 361 (2019) 1352–1362.
[33] F. Deng, Q. Zhang, L. Yang, et al., Appl. Catal. B: Environ. 238 (2018) 61–69.
[34] Y. Hong, C. Li, B. Yin, et al., Chem. Eng. J. 338 (2018) 137–146.
[35] Y. Jia, S. Li, H. Ma, et al., J. Hazard. Mater. 382 (2020) 121121.
[36] M. Sun, T. Yan, Y. Zhang, et al., J. Colloid Interface Sci. 514 (2018) 240–249.
[37] M. Sun, Y. Wang, Y. Shao, et al., J. Colloid Interface Sci. 501 (2017) 123–132.
[38] H. Guan, Y. Feng, Mater. Lett. 143 (2015) 269–272.
[39] Y. Hu, D. Li, F. Sun, et al., J. Hazard. Mater. 301 (2016) 362–370.
[40] X. Xu, L. Meng, Y. Li, et al., Appl. Surf. Sci. 479 (2019) 410–422.
[41] L. Luo, X. Shen, L. Song, et al., J. Alloys Compd. 779 (2019) 599–608.
[42] B. Shao, X. Liu, Z. Liu, et al., Chem. Eng. J. 368 (2019) 730–745.
[43] L. Cai, G. Zhang, Y. Zhang, Y. Wei, CrystEngComm 20 (2018) 3647–3656.
[44] W. Luo, F. Li, Q. Li, et al., ACS Appl. Mater. Interfaces 10 (2018) 7201–7207.
[45] Y. Zhu, Y. Wang, Z. Chen, et al., Appl. Catal. A Gen. 498 (2015) 159–166.
[46] L. Yu, X. Zhang, G. Li, et al., Appl. Catal. B: Environ. 187 (2016) 301–309.
[47] F. Mu, Q. Cai, H. Hu, et al., Chem. Eng. J. 384 (2020) 123352.
[48] X. Han, X. He, L. Sun, et al., ACS Catal. 8 (2018) 3348–3356.
[49] B. Yang, K. Lv, Q. Li, J. Fan, M. Li, Appl. Surf. Sci. 495 (2019) 143561.